Table 3. *Diameter change during RH*

	Control		Catalase		L-NMMA		L-NMMA + Catalase	
	B	RH	B	RH	B	RH	B	RH
RH 20, μm								
WT	36±4	49±4†	36±4	44±4†	36±3	42±3*	36±4	38±3
Cu/Zn-SOD$^{-/-}$	36±4	48±5†	36±4	42±5†	36±4	38±4	36±3	38±4
RH 60, μm								
WT	40±4	55±4†	40±4	51±4†	40±5	47±4*	39±4	41±4
Cu/Zn-SOD$^{-/-}$	40±3	56±4†	40±3	51±4†	39±4	42±3	40±5	42±3

Values are means ± SE; *n*, number of arterioles per animal. *$P < 0.01$ vs. B.

human mesenteric microvessels. Subsequently, our laboratory (42) and others (23) have confirmed that endogenous H_2O_2 exerts important vasodilator effects in canine coronary microcirculation in vivo and in isolated human coronary microvessels, respectively. H_2O_2 can be formed from superoxide anions derived from several sources in endothelial cells, including endothelial NO synthase (eNOS), cyclooxygenase, lipoxygenase, cytochrome *P*-450 enzymes, and reduced NADP [NAD(P)H] oxidases. Gupte et al. (10) demonstrated that cytosolic NADH redox and Cu,Zn-SOD activity have important roles in controlling the inhibitory effects of superoxide anions derived from NADH oxidase. Morikawa et al. (24a, 25) have also demonstrated that endothelial Cu,Zn-SOD plays an important role in the synthesis of H_2O_2 in mouse and human mesenteric arteries in vitro.

In the present study, catalase or L-NMMA alone significantly, but not completely, inhibited the RH-induced vasodilatation of mesenteric arterioles in wild-type mice in vivo, whereas L-NMMA + catalase markedly attenuated the remaining vasodilatation. In contrast, in Cu,Zn-SOD$^{-/-}$ mice, L-NMMA alone significantly decreased the vasodilatation and blood flow in response to 20- and 60-s arterial occlusion (Figs. 1 and 2). These results obtained using a pencil-type CCD intravital microscope indicate that H_2O_2 exerts important vasodilator effects on mesenteric smaller arterioles during RH and that Cu,Zn-SOD plays an important role in the synthesis of endogenous H_2O_2 during RH in vivo. Koller and Bagi (14a) showed that RH in rat isolated coronary arterioles was sensitive to pressure/stretch and flow/shear stress. Miura et al. (23) also showed the important role of endogenous H_2O_2 in flow-induced vasodilatation of human coronary arterioles. Koller and Bagi (14a) also suggested that H_2O_2 contributes to the development of the early peak phase of RH but not the duration of reactive vasodilatation, whereas NO prolongs the later phase of RH in rat isolated coronary arterioles, suggesting that H_2O_2 released endogenously within the vascular wall changes hemodynamic forces. In the present study, peak blood flow was significantly decreased after catalase (Fig. 2), suggesting that flow-induced vasodilatation during the early phase of RH is indeed mediated by H_2O_2 in mouse mesenteric arterioles in vivo.

Compensatory vasodilator mechanism between H_2O_2 and NO. It is well known that coronary vascular tone is regulated by the interactions among hemodynamic forces and several endogenous vasodilators, including NO, H_2O_2, and adenosine (41a, 42). Koller and Bagi (14a) demonstrated that mechanosensitive mechanisms were activated by changes in pressure and flow/shear stress during RH in isolated coronary arterioles. A superoxide anion is dismutated to H_2O_2 by manganese SOD (Mn-SOD, mitochondrial matrix) and Cu,Zn-SOD. H_2O_2 diffuses across the mitochondrial membrane to act on vascular smooth muscle (45). Tsunoda et al. (35) demonstrated that Mn-SOD augmented RH during 60-s canine coronary ischemia and reperfusion. H_2O_2 generated in the arteriolar smooth muscle could cause the response of activation of cGMP in rat skeletal muscle arterioles (38). Kitakaze et al. (12) indicated that the augmentation of reactive hyperemic flow caused by SOD is attributed to the enhanced release of adenosine in canine coronary circulation. These endogenous vasodilators may play an important role in causing the compensatory vasodilatation of coronary microvessels during myocardial ischemia.

In the present study, endothelium-dependent vasodilatation during RH (in the presence of L-NMMA) was almost completely inhibited by catalase in wild-type mice. In the Cu,Zn-SOD$^{-/-}$ mice, vasodilatation during RH remained under the control condition but was almost completely inhibited by L-NMMA (Fig. 1). The RH-induced increase in blood flow (in the presence of indomethacin and L-NMMA) was significantly inhibited by catalase in the wild-type mice but not in Cu,Zn-SOD$^{-/-}$ mice (Fig. 2). RH-induced increase in blood flow (in the presence of indomethacin and L-NMMA) remained in Cu,Zn-SOD$^{-/-}$ mice (Fig. 2). H_2O_2 may compensate for the loss of action of NO. H_2O_2 produced by SOD other than Cu,Zn-SOD may compensate for the loss of action of Cu,Zn-SOD-derived H_2O_2.

Table 4. *Diameter change during administration of ACh and SNP*

	ACh				SNP			
	B	ACh 10^{-7}	ACh 10^{-6}	ACh 10^{-5}	B	SNP 10^{-7}	SNP 10^{-6}	SNP 10^{-5}
WT, μm	36±3	41±3*	45±3†	49±4†	35±4	39±4*	43±5†	46±5†
Cu/Zn-SOD$^{-/-}$, μm	36±4	38±4	41±4*	44±4†	34±4	38±4*	41±4†	44±4†

Values are means ± SE; *n*, number of arterioles per animal. *$P < 0.05$; †$P < 0.01$ vs. B.

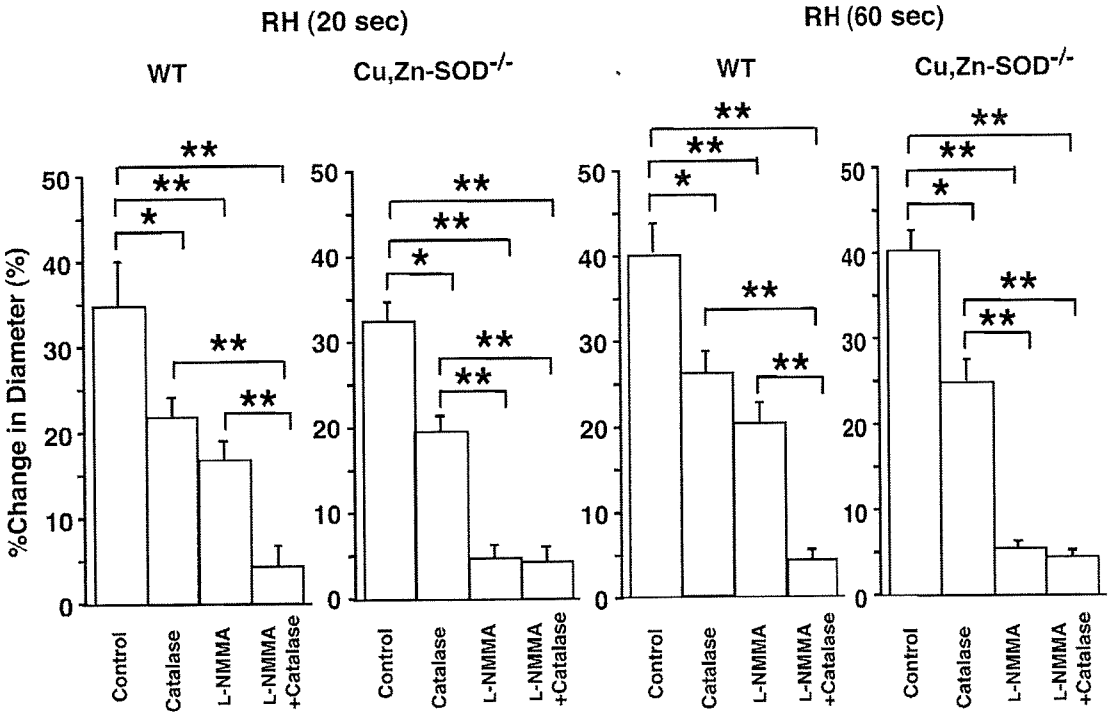

Fig. 1. Mesenteric vasodilatation during reactive hyperemia (RH). In the wild-type (WT) mice, vasodilatation during RH was inhibited by catalase or N^G-monomethyl-L-arginine (L-NMMA) and further inhibited by L-NMMA + catalase. In the Cu,Zn-SOD$^{-/-}$ mice (Cu,Zn-SOD$^{-/-}$), vasodilatation during RH was inhibited by catalase and markedly inhibited by L-NMMA, and the remaining response was not inhibited by catalase. The number of arterioles per animals used was 10/5 for each group. $*P < 0.05$; $**P < 0.01$.

Improvement of ACh-induced vasodilatation by Tempol in Cu,Zn-SOD$^{-/-}$ mice. It was previously reported that Tempol, a cell membrane-permeable SOD mimetic 4-hydroxy-2,2,6,6-tetramethylpiperidine-*N*-oxyl, decreased oxidative stress in the spontaneously hypertensive rat (31). In the present study, Tempol significantly improved the ACh-induced vasodilatation in Cu,Zn-SOD$^{-/-}$ mice, whereas catalase abolished the beneficial effect of Tempol (Fig. 3), indicating that the effect of Tempol was mediated by endogenous H_2O_2 in vivo. In contrast, Tempol had no enhancing effect on the ACh-induced vasodilatation in control mice (Fig. 3), suggesting that a sufficient amount of SOD is present in this strain. In Cu,Zn-SOD$^{-/-}$ mice, L-NMMA did not abolish the ACh-induced vasodilation, and the DCF-DA stain showed remaining fluorescent intensity (Fig. 4). Thus the residual vasodilatation could be caused by the following possible mechanisms. First, NO may also be synthesized in a nonenzymatic manner (27). Nonenzymatic synthesis of NO could occur in the presence of NADPH, glutathione, and L-cysteine, etc., opposing the effects of NOS inhibition (27). Second, the effects of L-NMMA may be limited since it is known that L-NMMA does not abolish NO production (1). H_2O_2 produced from vascular smooth muscle cells and other tissues may also contribute to the residual vasodilation (5, 30). Third, the contribution of other proposed

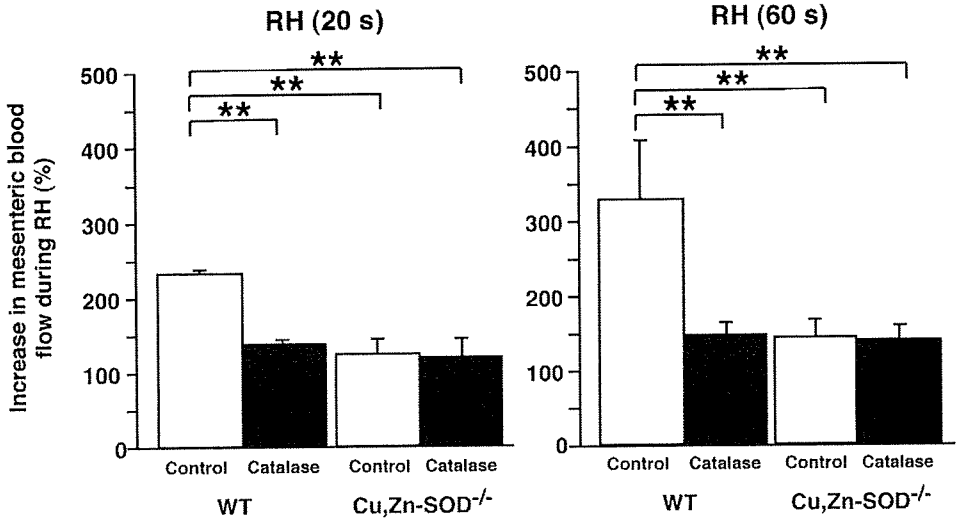

Fig. 2. The increase in mesenteric blood flow during RH. In the presence of indomethacin and L-NMMA, RH-induced increase in blood flow was sensitive to catalase in the WT mice, whereas in the Cu,Zn-SOD$^{-/-}$, the vasodilation was significantly reduced in control and was insensitive to catalase. The number of animals used was 5 for each group. $**P < 0.01$.

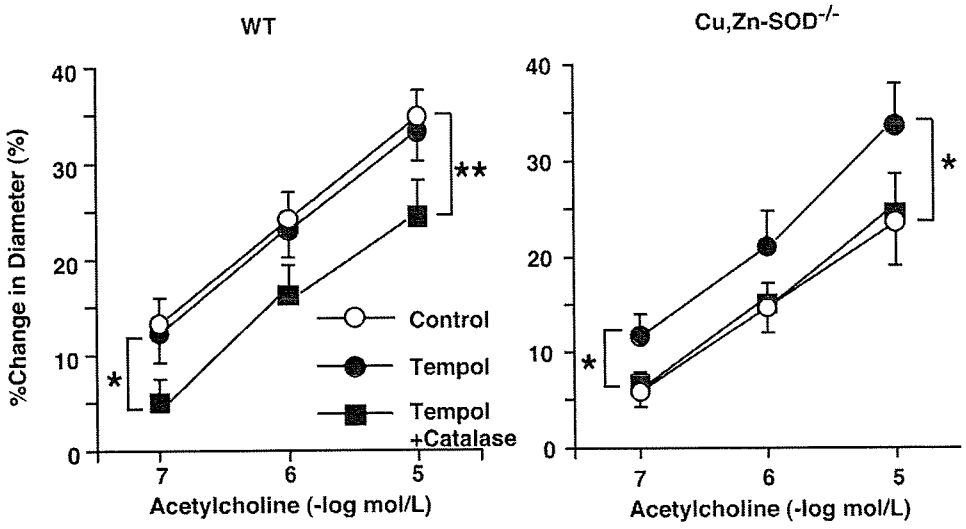

Fig. 3. Endothelium-dependent relaxations to ACh. In the WT mice, endothelium-dependent vasodilatation to ACh (in the presence of indomethacin and L-NMMA) was unchanged with Tempol but significantly inhibited by the addition of catalase. In the Cu,Zn-SOD$^{-/-}$, the vasodilation was significantly enhanced with Tempol, where the response was sensitive to the addition of catalase. The number of arterioles per animals used was 10/5 for each group. *P < 0.05; **P < 0.01.

EDHF candidates, such as P-450 metabolites (2, 3) and potassium ion (7), may contribute to the residual vasodilatation. Although RH and ACh have different mechanisms of vasodilator effects, they also share the same flow-induced vasodilator mechanism.

Endothelium-independent vasodilatation in Cu,Zn-SOD$^{-/-}$ mice. Microvascular dysfunction in hypercholesterolemic rats was confined to the endothelium because the dilator response to SNP and adenosine was unchanged (37). In the present study, endothelium-independent vasodilatation in response to SNP was comparable between the two genotypes, suggesting that vasodilatation properties of vascular smooth muscle cells were preserved in the Cu,Zn-SOD$^{-/-}$ mice in vivo.

Detection of vascular H_2O_2 and NO production. Our laboratory (41a) has recently demonstrated that vascular production of H_2O_2 and NO after ischemia-reperfusion is enhanced in small coronary arteries and arterioles in vivo, respectively. It was previously shown that a ACh-induced increase in fluorescence intensity in endothelial cells of the mesenteric artery is significantly reduced in Cu,Zn-SOD$^{-/-}$ mice (25). In the present study, vascular H_2O_2 production, as assessed by DCF-DA fluorescent intensity in mesenteric arterioles, was markedly impaired

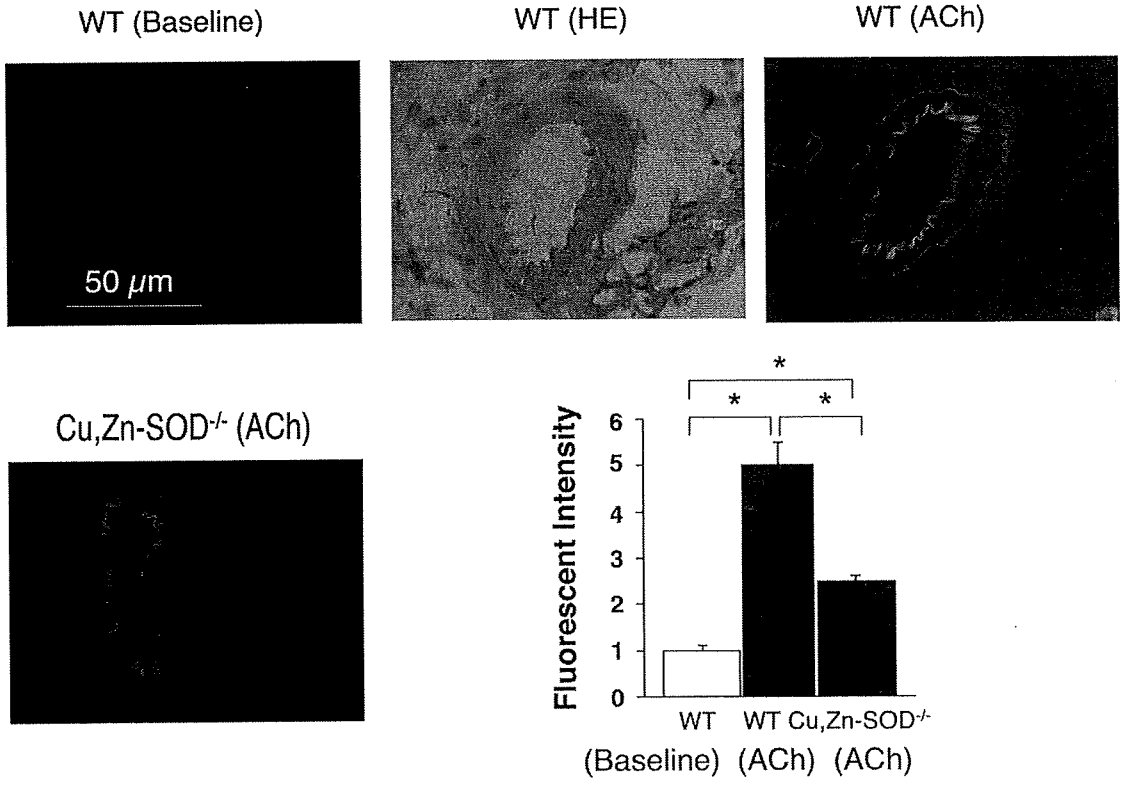

Fig. 4. Detection of vascular H_2O_2 production. Vascular H_2O_2 production in mesenteric arterioles was significantly increased in response to ACh in WT mice but markedly impaired in Cu,Zn-SOD$^{-/-}$. The number of arterioles per animals used was 10/5 for each group. *P < 0.05. HE, Hematoxylin eosin.

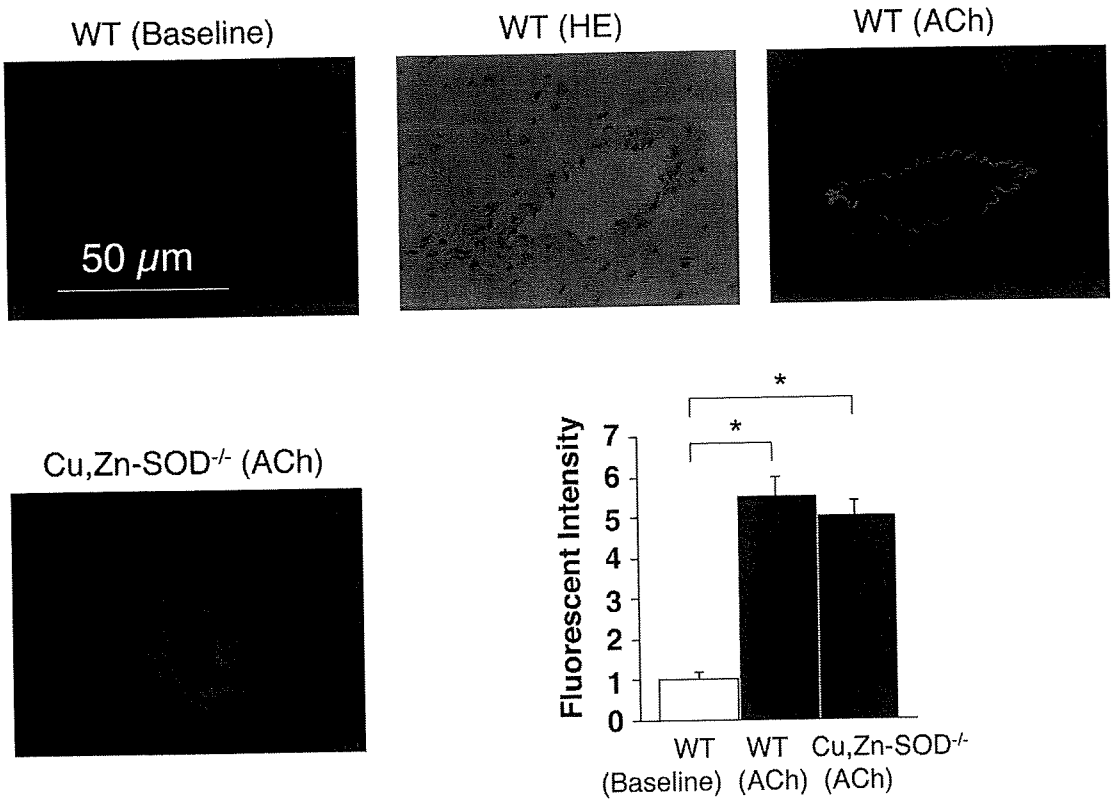

Fig. 5. Detection of vascular nitric oxide (NO) production. Vascular NO production in mesenteric arterioles was significantly increased in response to ACh in WT mice and unaltered in Cu,Zn-SOD$^{-/-}$. The number of arterioles per animals used was 10/5 for each group. *$P < 0.05$.

in Cu,Zn-SOD$^{-/-}$ mice (Fig. 4). These findings indicate that endothelial production of H_2O_2 is significantly impaired in Cu,Zn-SOD$^{-/-}$ mice, confirming the importance of the enzyme in endothelial synthesis of H_2O_2.

In the previous study by Morikawa et al. (25), eNOS protein expression was comparable between Cu,Zn-SOD$^{-/-}$ and wild-type mice. In the present study, vascular NO production in small mesenteric artery was unaltered in Cu,Zn-SOD$^{-/-}$ mice compared with wild-type mice (Fig. 5). NO could compensate for the loss of action of H_2O_2, although there are still many uncertainties about the local cellular dynamics of superoxide anions and NO.

Study limitations. Several limitations should be mentioned for the present study. First, we estimated blood flow in the mesenteric circulation using microspheres. We were unable to calculate the absolute values of local blood flow or shear stress because of the methodological limitations. However, since the flow measurement with microspheres was performed at the end of the experiments, it should not have influenced other results. Second, we used Cu,Zn-SOD$^{-/-}$ mice in the present study, where unknown compensatory mechanisms may be operative, and we were unable to elucidate the mechanism(s) for the remaining EDHF-mediated responses in those mice.

Clinical implications. RH is an important regulatory mechanism of the cardiovascular system, reflecting the flow reserve in response to a brief period of cessation of flow. An impaired flow reserve in resistance vessels is a hallmark of microvascular dysfunction with coronary risk factors. Hypertension is associated with structural alterations in the microcirculation and a reduced endothelium-dependent dilation in conduit arteries (19). It is well known that abnormality in Cu,Zn-SOD is noted in several diseases, including hypertension and diabetes mellitus (36, 39).

In conclusion, endogenous H_2O_2 exerts important vasodilator effects of mesenteric smaller arterioles during RH, especially at the low level of NO, and that Cu,Zn-SOD plays an important role in the synthesis of endogenous H_2O_2 during RH in vivo.

GRANTS

This work was supported in part by the Japanese Ministry of Education, Science, Sports, Culture, and Technology (Tokyo, Japan) Grants 16209027 (to H. Shimokawa), 16300164, and 19300167 (to T. Yada), the Program for Promotion of Fundamental Studies in Health Sciences of the Organization for Pharmaceutical Safety and Research of Japan (to H. Shimokawa), and Takeda Science Foundation 2002 (to T. Yada).

REFERENCES

1. **Amezcua JL, Palmer RM, de Souza BM, Moncada S.** Nitric oxide synthesized from L-arginine regulates vascular tone in the coronary circulation of the rabbit. *Br J Pharmacol* 97: 1119–1124, 1989.
2. **Bauersachs J, Hecker M, Busse R.** Display of the characteristics of endothelium-derived hyperpolarizing factor by a cytochrome P450-derived arachidonic acid metabolite in the coronary microcirculation. *Br J Pharmacol* 113: 1548–1553, 1994.
3. **Campbell WB, Gebremedhin D, Pratt PF, Harder DR.** Identification of epoxyeicosatrienoic acids as an endothelium-derived hyperpolarizing factor. *Circ Res* 78: 415–423, 1996.
4. **Chen G, Suzuki H, Weston AH.** Acetylcholine releases endothelium-derived hyperpolarizing factor and EDRF from blood vessels. *Br J Pharmacol* 95: 1165–1174, 1988.
5. **Chen Y, Pearlman A, Luo Z, Wilcox CS.** Hydrogen peroxide mediates a transient vasorelaxation with Tempol during oxidative stress. *Am J Physiol Heart Circ Physiol* 293: H2085–H2092, 2007.

6. **Coffman JD, Gregg DE.** Reactive hyperemia characteristics of the myocardium. *Am J Physiol* 199: 1143–1149, 1960.
7. **Edwards G, Dora KA, Gardener MJ, Garland CJ, Weston AH.** K^+ is an endothelium-derived hyperpolarizing factor in rat arteries. *Nature* 396: 269–272, 1998.
8. **Feletou M, Vanhoutte PM.** Endothelium-dependent hyperpolarization of canine smooth muscle. *Br J Pharmacol* 93: 515–524, 1988.
9. **Feletou M, Vanhoutte PM.** Endothelium-derived hyperpolarizing factor: where are we now? *Arterioscler Thromb Vasc Biol* 26: 1215–1225, 2006.
10. **Gupte SA, Rupawalla T, Mohazzab-H KM, Wolin MS.** Regulation of NO-elicited pulmonary artery relaxation and guanylate cyclase activation by NADH oxidase and SOD. *Am J Physiol Heart Circ Physiol* 276: H1535–H1542, 1999.
11. **Kanatsuka H, Sekiguchi N, Sato K, Akai K, Wang Y, Komaru T, Ashikawa K, Takishima T.** Microvascular sites and mechanisms responsible for reactive hyperemia in the coronary circulation of the beating canine heart. *Circ Res* 71: 912–922, 1992.
12. **Kitakaze M, Hori M, Takashima S, Iwai K, Sato H, Inoue M, Kitabatake A, Kamada T.** Superoxide dismutase enhances ischemia-induced reactive hyperemic flow and adenosine release in dogs. A role of 5′-nucleotidase activity. *Circ Res* 71: 558–566, 1992.
13. **Kiyooka T, Hiramatsu O, Shigeto F, Nakamoto H, Tachibana H, Yada T, Ogasawara Y, Kajiya M, Morimoto T, Morizane Y, Mohri S, Shimizu J, Ohe T, Kajiya F.** Direct observation of epicardial coronary capillary hemodynamics during reactive hyperemia and during adenosine administration by intravital video microscopy. *Am J Physiol Heart Circ Physiol* 288: H1437–H1443, 2005.
14. **Kobayashi N, Kobayashi K, Kouno K, Horinaka S, Yagi S.** Effects of intra-atrial injection of colored microspheres on systemic hemodynamics and regional blood flow in rats. *Am J Physiol Heart Circ Physiol* 266: H1910–H1917, 1994.

14a. **Koller A, Bagi Z.** Nitric oxide and H_2O_2 contribute to reactive dilation of isolated coronary arterioles. *Am J Physiol Heart Circ Physiol* 287: H2461–H2467, 2004.

15. **Koller A, Sun D, Kaley G.** Role of shear stress and endothelial prostaglandins in flow- and viscosity-induced dilation of arterioles in vitro. *Circ Res* 72: 1276–1284, 1993.
17. **Kopkan L, Castillo A, Navar LG, Majid DS.** Enhanced superoxide generation modulates renal function in ANG II-induced hypertensive rats. *Am J Physiol Renal Physiol* 290: F80–F86, 2006.
18. **Kuo L, Davis MJ, Chilian WM.** Endothelium-dependent, flow-induced dilation of isolated coronary arterioles. *Am J Physiol Heart Circ Physiol* 259: H1063–H1070, 1990.
19. **Lauer T, Heiss C, Preik M, Balzer J, Hafner D, Strauer BE, Kelm M.** Reduction of peripheral flow reserve impairs endothelial function in conduit arteries of patients with essential hypertension. *J Hypertens* 23: 563–569, 2005.

19a. **Matoba T, Shimokawa H, Kubota H, Morikawa K, Fujiki T, Kunihiro I, Mukai Y, Hirakawa Y, Takeshita A.** Hydrogen peroxide is an endothelium-derived hyperpolarizing factor in human mesenteric arteries. *Biochem Biophys Res Commun* 290: 909–913, 2002.

19b. **Matoba T, Shimokawa H, Morikawa K, Kubota H, Kunihiro I, Urakami-Harasawa L, Mukai Y, Hirakawa Y, Akaike T, Takeshita A.** Electron spin resonance detection of hydrogen peroxide as an endothelium-derived hyperpolarizing factor in porcine coronary microvessels. *Arterioscler Thromb Vasc Biol* 23: 1224–1230, 2003.

20. **Matoba T, Shimokawa H, Nakashima M, Hirakawa Y, Mukai Y, Hirano K, Kanaide H, Takeshita A.** Hydrogen peroxide is an endothelium-derived hyperpolarizing factor in mice. *J Clin Invest* 106: 1521–1530, 2000.
23. **Miura H, Bosnjak JJ, Ning G, Saito T, Miura M, Gutterman DD.** Role for hydrogen peroxide in flow-induced dilation of human coronary arterioles. *Circ Res* 92: e31–e40, 2003.
24. **Mori H, Haruyama S, Shinozaki Y, Okino H, Iida A, Takanashi R, Sakuma I, Husseini WK, Payne BD, Hoffman JI.** New nonradioactive microspheres and more sensitive X-ray fluorescence to measure regional blood flow. *Am J Physiol Heart Circ Physiol* 263: H1946–H1957, 1992.

24a. **Morikawa K, Fujiki T, Matoba T, Kubota H, Hatanaka M, Takahashi S, Shimokawa H.** Important role of superoxide dismutase in EDHF-mediated responses of human mesenteric arteries. *J Cardiovasc Pharmacol* 44: 552–556, 2004.

25. **Morikawa K, Shimokawa H, Matoba T, Kubota H, Akaike T, Talukder MA, Hatanaka M, Fujiki T, Maeda H, Takahashi S, Takeshita A.** Pivotal role of Cu,Zn-superoxide dismutase in endothelium-dependent hyperpolarization. *J Clin Invest* 112: 1871–1879, 2003.
27. **Moroz LL, Norby SW, Cruz L, Sweedler JV, Gillette R, Clarkson RB.** Non-enzymatic production of nitric oxide (NO) from NO synthase inhibitors. *Biochem Biophys Res Commun* 253: 571–576, 1998.
28. **Olsson RA.** Myocardial reactive hyperemia. *Circ Res* 37: 263–270, 1975.
29. **Pawlik WW, Obuchowicz R, Pawlik MW, Sendur R, Biernat J, Brzozowski T, Konturek SJ.** Histamine H_3 receptors modulate reactive hyperemia in rat gut. *J Physiol Pharmacol* 55: 651–661, 2004.
30. **Saitoh S, Zhang C, Tune JD, Potter B, Kiyooka T, Rogers PA, Knudson JD, Dick GM, Swafford A, Chilian WM.** Hydrogen peroxide: a feed-forward dilator that couples myocardial metabolism to coronary blood flow. *Arterioscler Thromb Vasc Biol* 26: 2614–2621, 2006.
31. **Schnackenberg CG, Wilcox CS.** Two-week administration of Tempol attenuates both hypertension and renal excretion of 8-Iso prostaglandin F_{2alpha}. *Hypertension* 33: 424–428, 1999.
32. **Shimokawa H.** Primary endothelial dysfunction: atherosclerosis. *J Mol Cell Cardiol* 31: 23–37, 1999.
33. **Takamura Y, Shimokawa H, Zhao H, Igarashi H, Egashira K, Takeshita A.** Important role of endothelium-derived hyperpolarizing factor in shear stress-induced endothelium-dependent relaxations in the rat mesenteric artery. *J Cardiovasc Pharmacol* 34: 381–387, 1999.
34. **Taylor HJ, Chaytor AT, Evance WH, Griffith TM.** Inhibition of the gap junctional component of endothelium-dependent relaxations in rabbit iliac artery by 18-alpha glycyrrhetinic acid. *Br J Pharmacol* 125: 1–3, 1998.
35. **Tsunoda R, Okumura K, Ishizaka H, Matsunaga T, Tabuchi T, Tayama S, Yasue H.** Enhancement of myocardial reactive hyperemia with manganese-superoxide dismutase: role of endothelium-derived nitric oxide. *Cardiovasc Res* 31: 537–545, 1996.
36. **Uchimura K, Nagasaka A, Hayashi R, Makino M, Nagata M, Kakizawa H, Kobayashi T, Fujiwara K, Kato T, Iwase K, Shinohara R, Kato K, Itoh M.** Changes in superoxide dismutase activities and concentrations and myeloperoxidase activities in leukocytes from patients with diabetes mellitus. *J Diabetes Complications* 13: 264–270, 1999.
37. **VanTeeffelen JW, Constantinescu AA, Vink H, Spaan JA.** Hypercholesterolemia impairs reactive hyperemic vasodilation of 2A but not 3A arterioles in mouse cremaster muscle. *Am J Physiol Heart Circ Physiol* 289: H447–H454, 2005.
38. **Wolin MS, Rodenburg JM, Messina EJ, Kaley G.** Similarities in the pharmacological modulation of reactive hyperemia and vasodilation to hydrogen peroxide in rat skeletal muscle arterioles: effects of probes for endothelium-derived mediators. *J Pharmacol Exp Ther* 253: 508–512, 1990.
39. **Wu R, Millette E, Wu L, de Champlain J.** Enhanced superoxide anion formation in vascular tissues from spontaneously hypertensive and desoxycorticosterone acetate-salt hypertensive rats. *J Hypertens* 19: 741–748, 2001.
40. **Yada T, Hiramatsu O, Kimura A, Goto M, Ogasawara Y, Tsujioka K, Yamamori S, Ohno K, Hosaka H, Kajiya F.** In vivo observation of subendocardial microvessels of the beating porcine heart using a needle-probe videomicroscope with a CCD camera. *Circ Res* 72: 939–946, 1993.
41. **Yada T, Hiramatsu O, Kimura A, Tachibana H, Chiba Y, Lu S, Goto M, Ogasawara Y, Tsujioka K, Kajiya F.** Direct in vivo observation of subendocardial arteriolar response during reactive hyperemia. *Circ Res* 77: 622–631, 1995.

41a. **Yada T, Shimokawa H, Hiramatsu O, Haruna Y, Morita Y, Kashihara N, Shinozaki Y, Mori H, Goto M, Ogasawara Y, Kajiya F.** Cardioprotective role of endogenous hydrogen peroxide during ischemia-reperfusion injury in canine coronary microcirculation in vivo. *Am J Physiol Heart Circ Physiol* 291: H1138–H1146, 2006.

42. **Yada T, Shimokawa H, Hiramatsu O, Kajita T, Shigeto F, Goto M, Ogasawara Y, Kajiya F.** Hydrogen peroxide, an endogenous endothelium-derived hyperpolarizing factor, plays an important role in coronary autoregulation in vivo. *Circulation* 107: 1040–1045, 2003.
44. **Yada T, Shimokawa H, Hiramatsu O, Shinozaki Y, Mori H, Goto M, Ogasawara Y, Kajiya F.** Important role of endogenous hydrogen peroxide in pacing-induced metabolic coronary vasodilatation in dogs in vivo. *J Am Coll Cardiol* 50: 1272–1278, 2007.
45. **Zhang DX, Gutterman DD.** Mitochondrial reactive oxygen species-mediated signaling in endothelial cells. *Am J Physiol Heart Circ Physiol* 292: H2023–H2031, 2007.

Jpn. J. Med. Phys. Vol. 27 No. 4: 163–171 (2008)

研究論文

X-ray Spectra from a Brass-target Plasma Triode

Eiichi SATO[1]*, Haruo OBARA[2], Toshiyuki ENOMOTO[3], Etsuro TANAKA[4], Hidezo MORI[5], Toshiaki KAWAI[6], Toshio ICHIMARU[7], Akira OGAWA[8], Shigehiro SATO[9], Kazuyoshi TAKAYAMA[10] and Jun ONAGAWA[11]

[1] *Department of Physics, Iwate Medical University*
[2] *Department of Radiological Technology, College of Medical Science, Tohoku University*
[3] *The 3rd Department of Surgery, Toho University School of Medicine*
[4] *Department of Nutritional Science, Faculty of Applied Bioscience, Tokyo University of Agriculture*
[5] *Department of Cardiac Physiology, National Cardiovascular Center Research Institute*
[6] *Electron Tube Division #2, Hamamatsu Photonics K. K.*
[7] *Department of Radiological Technology, School of Health Sciences, Hirosaki University*
[8] *Department of Neurosurgery, School of Medicine, Iwate Medical University*
[9] *Department of Microbiology, School of Medicine, Iwate Medical University*
[10] *Tohoku University Biomedical Engineering Research Organization*
[11] *Department of Electronics, Faculty of Engineering, Tohoku Gakuin University*

Research Code No.: 200, 204.1
Keywords: Flash x-ray, Brass target, Weakly ionized linear plasma, Characteristic x-rays, Absorption of zinc Kβ rays

Abstract

In this paper, we describe a recently developed table-top plasma x-ray generator utilizing a brass-target triode, which we used in preliminary experiments for the superposition of K-series characteristic x-rays in weakly ionized plasma and for producing their higher harmonics. In the plasma flash x-ray generator, a 200 nF condenser was charged, and flash x-rays were produced by discharging. The x-ray tube was a demountable triode with a brass target containing 65% copper and 35% zinc by weight, and a turbomolecular pump evacuated air from the tube with a pressure of 1 mPa. Target evaporation led to the formation of weakly ionized linear plasma, consisting of metal ions and electrons, around the rod target, and intense characteristic x-rays were produced. At a charging voltage of 50 kV, the maximum tube voltage was almost equal to the charging voltage of the main condenser, and the peak current was 15 kA. When the charging voltage was increased, the linear plasma formed, and the K-series characteristic x-ray intensities of zinc Kα, copper Kβ, and copper Kβ lines increased substantially. On the other hand, hardly any zinc Kβ lines were detected. In particular, we confirmed the irradiation of the second unsharp harmonics of the fundamental Kα lines of copper and zinc. The x-ray pulse widths were 700 ns, and the time-integrated x-ray intensity was 1.2 mGy at 1.0 m per pulse with a charging voltage of 50 kV.

Received May 17, 2007; revision accepted October 25, 2007

*岩手医科大学共通教育センター物理学科〔〒028–3694 岩手県紫波郡矢巾町西徳田2–1–1〕: Department of Physics, Iwate Medical University
E-mail: dresato@iwate-med.ac.jp

1. Introduction

Synchrotrons produce monochromatic parallel beams using single crystals, and the photon energy is selected by Bragg's angle. In particular, the beams with photon energies of approximately 35 keV have been employed for enhanced K-edge angiography[1-3] using iodine contrast media, because iodine media with a K-edge of 33.2 keV absorb the beams effectively. Thus, we have developed a steady state cerium x-ray generator[4-6] and have succeeded in carrying out cone-beam enhanced angiography using cerium K-series characteristic x-rays.

Conventional flash x-ray generators[7] utilize high-voltage condensers and cold-cathode x-ray tubes, and produce extremely short x-ray pulses with durations of less than 1 μs. For use in biomedical radiography, we have developed several different flash x-ray generators[8-10] corresponding to specific radiographic objectives, and have succeeded in producing clean K-series characteristic x-rays of nickel and copper from a weakly ionized linear plasma using a plasma triode[11-14]. We have confirmed the irradiations of clean K-series characteristic x-rays of molybdenum using a compact flash x-ray generator with a disk-cathode diode[15,16], and we have developed an intense plasma diode to produce high-photon-energy characteristic x-rays of molybdenum, cerium[17], gadolinium, tantalum[18] and tungsten[19]. In particular, the tantalum and tungsten Kα rays have been applied to perform high-speed K-edge angiography using gadolinium-based contrast media.

In order to carry out wide-photon-energy or energy subtraction radiography, we are very interested in the variations of characteristic x-ray intensities from evaporating plasma target. In particular, the absorption of K-series characteristic x-rays in the plasma consisting of electrons and two-element metal ions requires investigations, since all K-rays of two elements are produced from the two-element solid alloy target. Furthermore, because we have confirmed the irradiation of higher harmonic hard x-rays using nickel and copper targets, the x-ray spectra with photon energies beyond the K-edges should be measured.

In this paper, we describe a recently developed table-top plasma x-ray generator utilizing a brass-target triode. We used it to carry out preliminary experiments for the superposition of K-series characteristic x-rays in weakly ionized plasma and for producing their higher harmonics.

2. Generator

Figure 1 shows a block diagram of a high-intensity plasma flash x-ray generator. This generator consists of the following essential components: a high-voltage power supply, a high-voltage condenser with a capacity of 200 nF, a turbomolecular pump, a krytron pulse generator as a trigger device, and a flash x-ray tube. A low-impedance transmission line is employed in order to increase the maximum tube current in the generator. The high-voltage main condenser is charged to 50 kV by the power supply, and electric charges in the condenser are discharged to the tube after triggering the cathode electrode with the trigger device. The plasma flash x-rays are then produced.

The x-ray tube is a demountable cold-cathode triode that is connected to the turbomolecular pump with a pressure of approximately 1

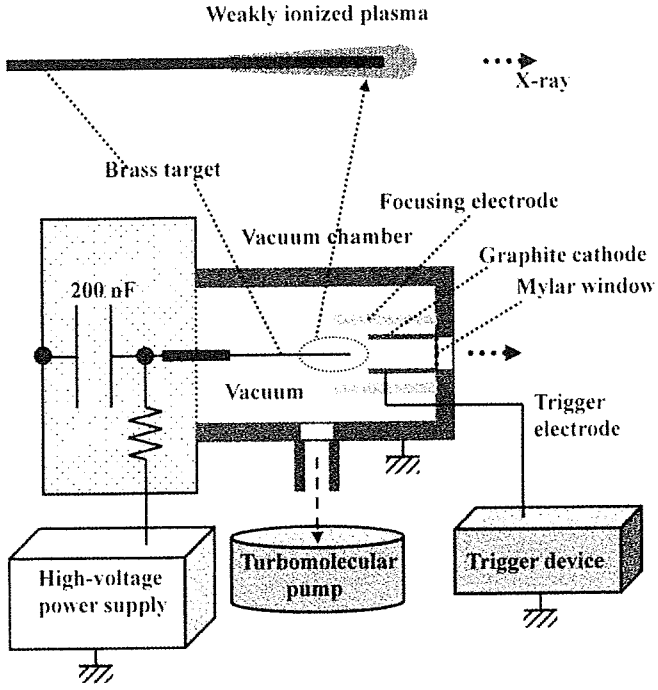

Fig. 1　Block diagram including the electric circuit of the high-intensity plasma flash x-ray generator.

mPa. This tube consists of the following major parts: a pipe-shaped graphite cathode with a bore diameter of 10.0 mm, a trigger electrode made from copper wire, a brass focusing electrode, a stainless steel vacuum chamber, a nylon insulator, a polyethylene terephthalate (Mylar) x-ray window 0.25 mm in thickness, and a 4.0-mm-diameter rod brass target containing 65% copper and 35% zinc by weight. The distance between the target and cathode is 20 mm, and the trigger electrode is set in the cathode electrode. As electron beams from the cathode are roughly converged to the target by the focusing electrode, evaporation leads to the formation of a weakly ionized linear plasma, consisting of metal ions and electrons, around the target.

3. Characteristics

3.1. Tube voltage and current

Tube voltage and current were measured by a high-voltage divider with an input impedance of 1 GΩ and a current transformer, respectively. Figure 2 shows the time relation between the tube voltage and current. The tube voltage and current roughly displayed damped oscillations at the indicated charging voltages. When the charging voltage was increased, both the maximum tube voltage and current increased. At a charging voltage of 50 kV, the maximum tube voltage was almost equal to the charging voltage of the main condenser, and the maximum tube current was 15 kA.

3.2. X-ray output

X-ray output pulse was detected using a combination of a plastic scintillator and a photomultiplier (Fig. 3). The x-ray pulse height substantially increased with corresponding increases in the charging voltage. The x-ray pulse widths were 700 ns, and the time-integrated x-ray intensity measured by a thermolu-

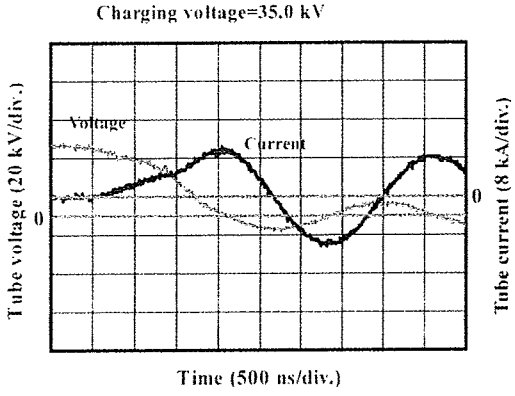

(a)

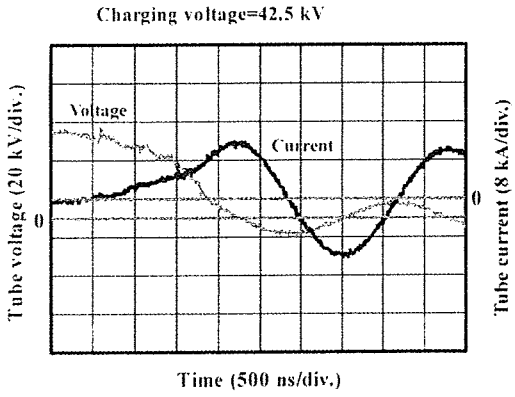

(b)

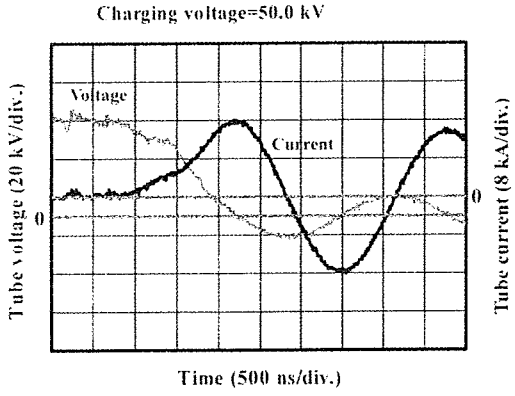

(c)

Fig. 2 Tube voltages and currents with a charging voltage of (a) 35.0 kV, (b) 42.5 kV and (c) 50.0 kV.

minescence dosimeter (Kyokko TLD Reader 1500 with MSO-S elements without energy compensation) had a value of 1.2 mGy at 1.0 m per pulse with a charging voltage of 50 kV.

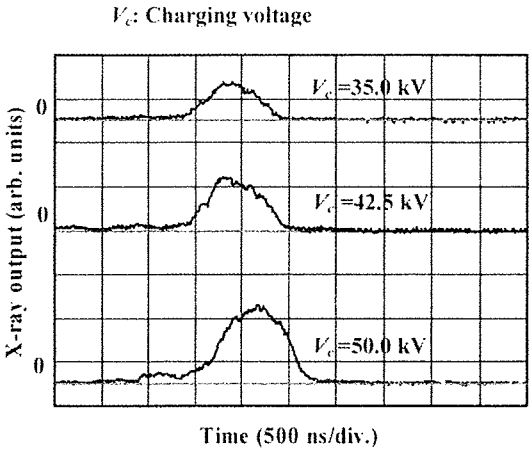

Fig. 3 X-ray outputs at the indicated conditions.

3.3. *X-ray source*

In order to roughly observe images of the plasma x-ray source in the detector plane, we employed a 100-μm-diameter pinhole camera and an x-ray film (Polaroid XR-7) (Fig. 4). When the charging voltage was increased, the plasma x-ray source grew, and both spot dimension and intensity increased. Because the x-ray intensity was the highest at the center of the target, both the dimension and intensity decreased according to both increases in the thickness of the filter for absorbing x-rays and decreases in the pinhole diameter. The minimum dimension was equal to the target diameter of 3.0 mm.

3.4. *X-ray spectra*

X-ray spectra from the plasma source were measured by a transmission-type spectrometer with a lithium fluoride curved crystal 0.5 mm in thickness. The spectra were taken by a computed radiography (CR) system (Konica Regius 150)[20] with a wide dynamic range, and relative x-ray intensity was calculated from Dicom digital data.

Figure 5 shows measured spectra from

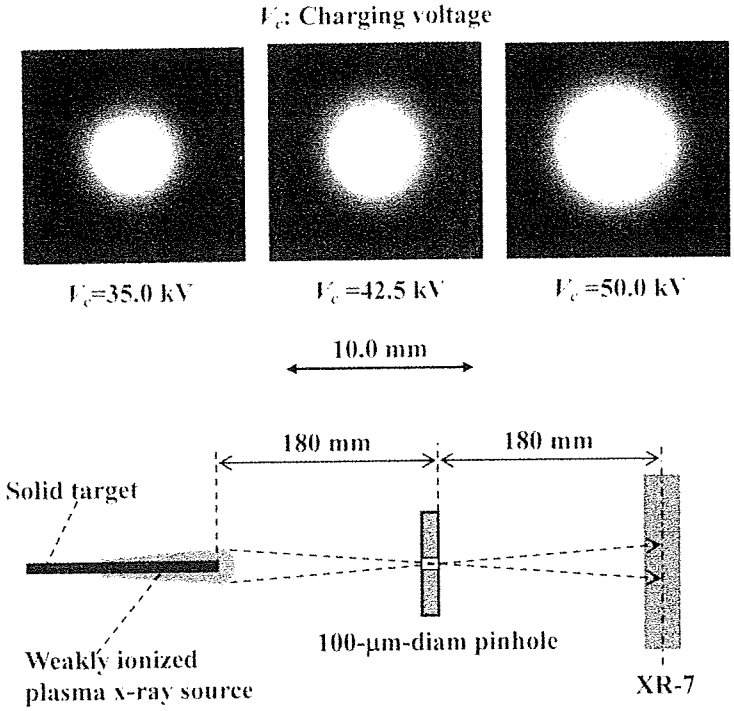

Fig. 4　Images of plasma x-ray source, and the experimental setup for imaging the source.

weakly ionized metal plasma. We observed clean copper Kα, copper Kβ and zinc Kα lines. However, zinc Kβ and bremsstrahlung rays were barely detected. The characteristic x-ray intensity substantially increased with increases in the charging voltage. In the high-photon-energy region, we confirmed the irradiation of the second unsharp harmonics of the fundamental K-lines of copper and zinc elements. The x-ray intensities of the harmonics increased with increases in the charging voltage, and the harmonic bremsstrahlung rays survived due to the x-ray resonation in the plasma.

4. Radiography

Plasma radiography was carried out with the CR system, and the charging voltage and the distance were 50 kV and 1.2 m, respectively.

Figure 6 shows radiograms of tungsten wires coiled around a pipe made of polymethyl methacrylate. Although the image contrast increased with increases in the wire diameter, a 50-μm-diameter wire could be observed. Next, the image of aluminum grains falling into a polypropylene beaker from a glass test tube is shown in Fig. 7. Because the x-ray duration was approximately 700 ns, the stop-motion image of grains could be obtained. Figure 8 shows angiograms of a rabbit thigh obtained utilizing iodine-based microspheres of 15 μm in diameter. In the angiography, a 100-μm-diam tungsten wire was used for determining the diameter of blood vessels, and fine blood vessels of about 100 μm were clearly visible.

5. Conclusions and Outlook

Regarding the spectrum measurement, although we confirmed clean copper Kα copper Kβ and zinc Kα lines, zinc Kβ lines were

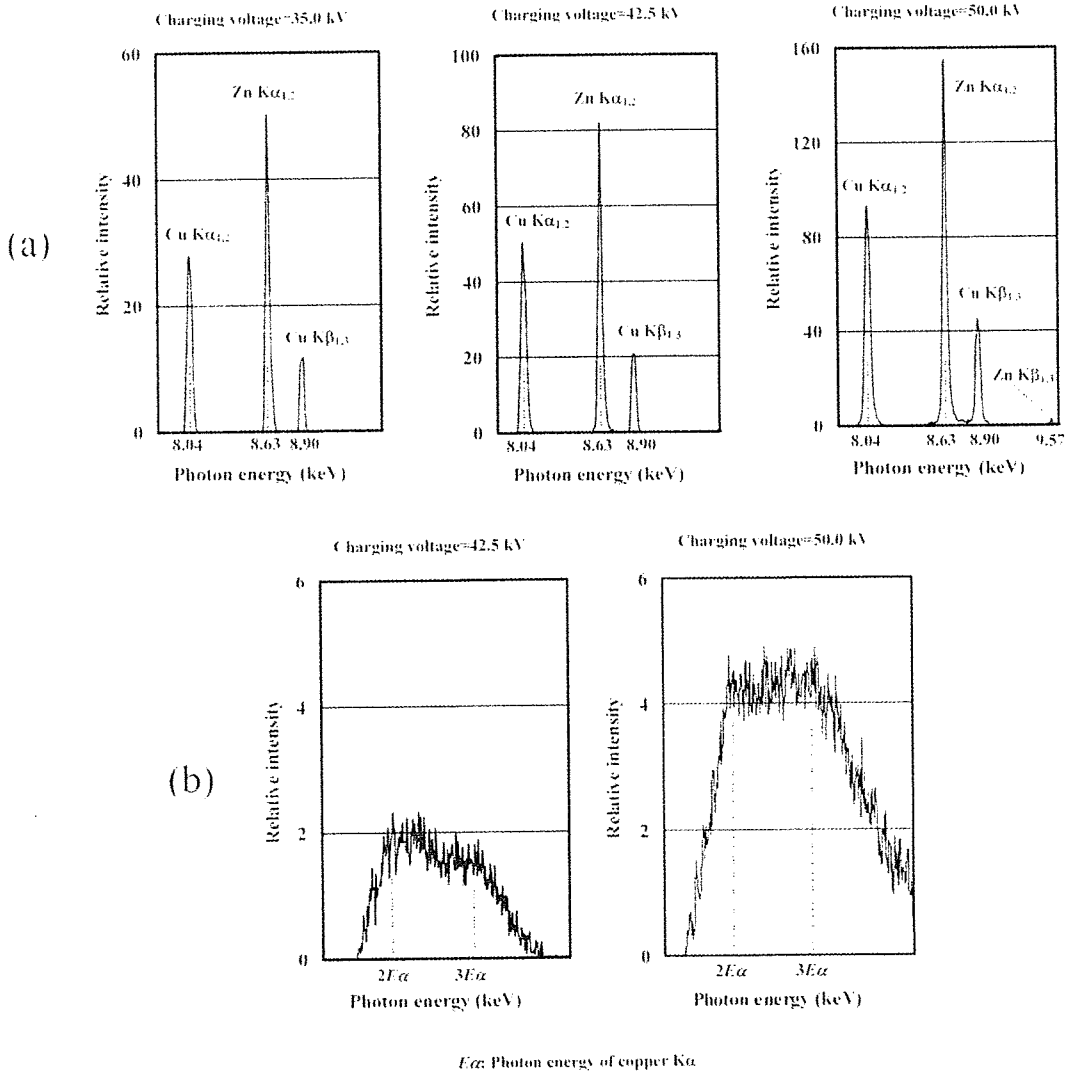

Fig. 5 X-ray spectra at the indicated conditions. (a) Characteristic x-rays and (b) bremsstrahlung x-rays.

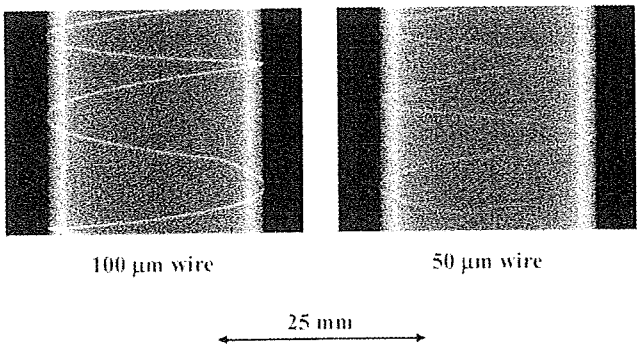

Fig. 6 Radiograms of tungsten wires coiled around pipes made of polymethyl methacrylate.

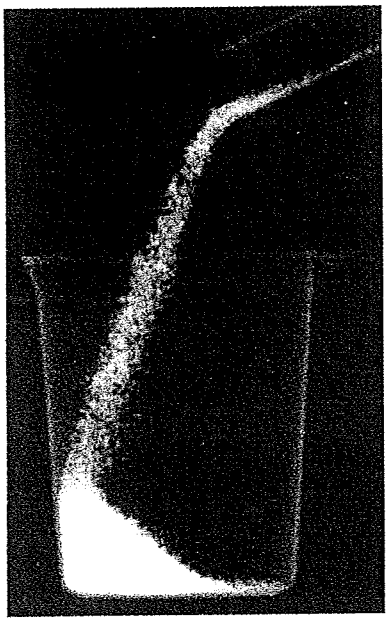

Fig. 7　Radiogram of aluminum grains falling from a glass test tube.

barely observed. Because the weakly ionized zinc plasma transmitted zinc Kβ lines easily, these lines were absorbed by the copper plasma. In the high-photon-energy region, we could not observe clean higher harmonics, and bremsstrahlung x-rays with photon energies of approximately $2E_{\gamma}$ were left in cases where high charging voltages beyond 40 kV were applied.

From the experimental results, we saw that the x-ray spectra with photon energies just beyond the copper K-edge were absorbed effectively by the copper plasma, and zinc Kβ rays would be useful for producing copper fluorescent rays. Next, we would like to obtain results using a capillary-type target for forming weakly ionized linear plasma.

In this research, we obtained sufficient characteristic x-ray intensity per pulse for CR radiography, and the generator produced number

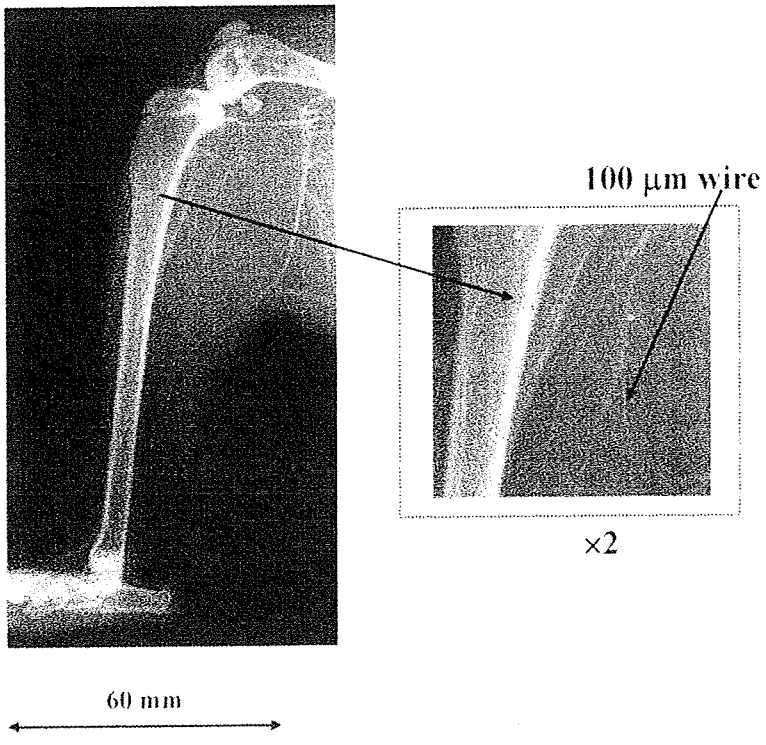

Fig. 8　Angiogram of a rabbit thigh.

of characteristic photons was approximately 1×10^{8} photons·cm^{-2} at 1.0 m per pulse. In addition, since the photon energy of characteristic x-rays can be controlled by changing target elements, various quasi-monochromatic high-speed radiographies, such as flash energy subtraction radiography using a metal filter and wide-photon-energy radiography, will be possible.

Acknowledgments

This work was supported by Grants-in-Aid for Scientific Research and Advanced Medical Scientific Research from MECSST, Health and Labor Sciences Research Grants, Grants from the Keiryo Research Foundation, The Promotion and Mutual Aid Corporation for Private Schools of Japan, the Japan Science and Technology Agency (JST), and the New Energy and Industrial Technology Development Organization (NEDO).

References

1) Thompson AC, Zeman HD, Brown GS et al.: First operation of the medical research facility at the NSLS for coronary angiography. Rev. Sci. Instrum. 63: 625–628, 1992
2) Mori H, Hyodo K, Tanaka E et al.: Small-vessel radiography in situ with monochromatic synchrotron radiation. Radiology 201: 173–177, 1996
3) Hyodo K, Ando M, Oku Y et al.: Development of a two-dimensional imaging system for clinical applications of intravenous coronary angiography using intense synchrotron radiation produced by a multipole wiggler. J. Synchrotron Radiat. 5: 1123–1126, 1998
4) Sato E, Tanaka E, Mori H et al.: Demonstration of enhanced K-edge angiography using a cerium target x-ray generator. Med. Phys. 31: 3017–3021, 2004
5) Sato E, Yamadera A, Tanaka E et al.: X-ray spectra from a cerium target and their application to cone beam K-edge angiography. Opt. Eng 44: 096502-1-6, 2005
6) Sato E, Tanaka E, Mori H et al.: Variations in cerium x-ray spectra and enhanced K-edge angiography. Jpn. J. Appl. Phys. 44: 8204–8209, 2005
7) Germer R: X-ray flash techniques. J. Phys. E. Sci. Instrum. 12: 336–350, 1979
8) Sato E, Kimura S, Kawasaki S et al.: Repetitive flash x-ray generator utilizing a simple diode with a new type of energy-selective function. Rev. Sci. Instrum. 61: 2343–2348, 1990
9) Sato E, Takahashi K, Sagae M et al.: Sub-kilohertz flash x-ray generator utilizing a glass-enclosed cold-cathode triode. Med. Biol. Eng. Comput. 32: 289–294, 1994
10) Takahashi K, Sato E, Sagae M et al.: Fundamental study on a long-duration flash x-ray generator with a surface-discharge triode. Jpn. J. Appl. Phys. 33: 4146–4151, 1994
11) Sato E, Hayasi Y, Germer R et al.: Irradiation of intense characteristic x-rays from weakly ionized linear molybdenum plasma. Jpn. J. Med. Phys. 23: 123–131, 2003
12) Sato E, Tanaka E, Mori H et al.: Clean monochromatic x-ray irradiation from weakly ionized linear copper plasma. Opt. Eng. 44: 049002-1-6, 2005
13) Sato E, Hayasi Y, Germer R et al.: X-ray spectra from weakly ionized linear copper plasma. Jpn. J. Appl. Phys. 45: 5301–5306, 2006
14) Sato E, Hayasi Y, Tanaka E et al.: Preliminary study for producing higher harmonic hard x-rays from weakly ionized nickel plasma. Rad. Phys. Chem. 75: 1812–1818, 2006
15) Sato E, Tanaka E, Mori H et al.: Compact monochromatic flash x-ray generator utilizing a disk-cathode molybdenum tube. Med. Phys. 32: 49–54, 2005
16) Sato E, Hayasi Y, Germer R et al.: Monochromatic flash x-ray generator utilizing a disk-cathode silver tube. Opt. Eng. 44: 096501-1-6, 2005
17) Sato E, Germer R, Tanaka E et al.: Quasi-monochromatic cerium flash angiography. SPIE 5580: 146–152, 2005

18) Sato E, Hayasi Y, Kimura K et al.: Enhanced K-edge angiography utilizing tantalum plasma x-ray generator in conjunction with gadolinium-based contrast media. Jpn. J. Appl. Phys. 44: 8716–8721, 2005

19) Sato E, Hayasi Y, Tanaka E et al.: K-edge angiography utilizing a tungsten plasma x-ray generator in conjunction with gadolinium-based contrast media. Rad. Phys. Chem. 75: 1841–1849, 2006

20) Sato E, Sato K, Tamakawa Y: Film-less computed radiography system for high-speed imaging. Ann. Rep. Iwate Med. Univ. Sch. Lib. Arts. Sci. 35: 13–23, 2000

Japanese Journal of Applied Physics
Vol. 47, No. 6, 2008, pp. 4772–4776

Magnification K-Edge Angiography Utilizing 100-μm-Focus Tungsten Tube and Gadolinium-Based Contrast Media

Yuichi SATO, Eiichi SATO[1], Shigeru EHARA, Toshiyuki ENOMOTO[2], Etsuro TANAKA[3], Hidezo MORI[4], Toshiaki KAWAI[5], Akira OGAWA[6], Shigehiro SATO[7], and Jun ONAGAWA[8]

Department of Radiology, School of Medicine, Iwate Medical University, 19-1 Uchimaru, Morioka 020-8505, Japan
[1]*Department of Physics, Iwate Medical University, 2-1-1 Nishitokuta, Yahaba, Iwate 028-3694, Japan*
[2]*The 3rd Department of Surgery, Toho University School of Medicine, 2-17-6 Ohashi, Meguro-ku, Tokyo 153-8515, Japan*
[3]*Department of Nutritional Science, Faculty of Applied Bioscience, Tokyo University of Agriculture, 1-1-1 Sakuragaoka, Setagaya-ku, Tokyo 156-8502, Japan*
[4]*Department of Cardiac Physiology, National Cardiovascular Center Research Institute, 5-7-1 Fujishirodai, Suita, Osaka 565-8565, Japan*
[5]*Electron Tube Division #2, Hamamatsu Photonics K.K., 314-5 Shimokanzo, Iwata, Shizuoka 438-0193, Japan*
[6]*Department of Neurosurgery, School of Medicine, Iwate Medical University, 19-1 Uchimaru, Morioka 020-8505, Japan*
[7]*Department of Microbiology, School of Medicine, Iwate Medical University, 19-1 Uchimaru, Morioka 020-8505, Japan*
[8]*Department of Electronics, Faculty of Engineering, Tohoku Gakuin University, 1-13-1 Chuo, Tagajo, Miyagi 985-8537, Japan*

(Received December 11, 2007; revised February 13, 2008; accepted February 22, 2008; published online June 13, 2008)

A microfocus X-ray tube is useful for performing magnification digital radiography. The 100-μm-focus X-ray generator consists of a main controller, for regulating tube voltage and current, and a tube unit with a high-voltage circuit and a fixed anode X-ray tube. The maximum tube voltage, current, and electric power were 106 kV, 0.5 mA, and 50 W, respectively. Using a 100-μm-thick tungsten filter, the X-ray intensity was 19.8 μGy/s at 1.0 m from the source with a tube voltage of 100 kV and a current of 0.50 mA. Since Kα rays from tungsten targets are absorbed effectively by gadolinium-based contrast media, these rays are useful for performing enhanced angiography. Magnification angiography was performed by threefold magnification imaging using a computed radiography system and the filter at a tube voltage of 100 kV. In angiography of nonliving animals, we observed fine blood vessels of approximately 100 μm with high contrasts.
[DOI: 10.1143/JJAP.47.4772]

KEYWORDS: angiography, gadolinium-based contrast media, 100-μm-focus X-ray tube, tungsten K-rays, magnification radiography

1. Introduction

Energy-selective imaging has been performed using monochromatic X-rays, and extremely clean monochromatic parallel beams have been formed using synchrotrons in conjunction with single silicon crystals. In particular, because these beams with photon energies just beyond the iodine K-absorption edge 33.2 keV are absorbed effectively by iodine-based contrast media, enhanced K-edge angiography[1–3] has been carried out.

To produce extremely high-dose-rate pulse X-rays, various flash X-ray generators have been developed.[4,5] In particular, weakly ionized plasma flash X-ray generators[6–8] are useful for producing intense clean K-series characteristic X-rays because bremsstrahlung X-rays are absorbed effectively by the plasma. However, it is difficult to generate steady-state X-rays because conventional flash tubes utilize cold cathodes.

Recently, a steady-state X-ray generator utilizing a cerium-target tube[9,10] has been developed and has been applied to enhanced K-edge angiography achieved with cerium Kα rays and iodine-based contrast media, since the Kα rays (34.6 keV) are absorbed effectively by iodine-based media. When a computed radiography (CR) system (Konica Minolta Regius 150)[11] with a sampling pitch of 87.5 μm is used for angiography, blood vessels of 100 μm in diameter are observed. However, the spatial resolution measured using a lead test chart is approximately 200 μm.

Kα rays from ytterbium, tantalum, and tungsten targets are absorbed effectively by gadolinium-based contrast media, and these flash Kα rays are useful for performing high-speed enhanced K-edge angiography[12,13] with X-ray durations less than 1 μs. As compared with iodine K-edge angiography, the absorbed dose can be decreased easily in cases in which gadolinium media are employed. Although X-ray angiographic techniques utilizing gadolinium media have been performed,[14,15] gadolinium K-edge angiography is useful for decreasing the absorbed dose using effective X-ray spectra.

The maximum densities of the gadolinium and iodine elements in liquid contrast media are 150 and 370 mg/mL, respectively, and it is difficult to improve the image contrast of blood vessels using gadolinium media. Lately, we have developed a highly sensitive X-ray computed tomography (CT) system[16] utilizing a cadmium telluride detector and have performed iodine K-edge CT angiography (CTA) with an iodine density of 4 mg/mL using optimum X-rays. To decrease the absorbed dose for patients in angiographic techniques including CTA,[17,18] we are very interested in gadolinium K-edge angiography achieved using steady-state tungsten Kα rays and low-density contrast media, and unnecessary bremsstrahlung X-rays should be absorbed using a metal filter in enhanced angiography.

Microfocus X-ray tubes have been applied to phase contrast radiography utilizing magnification imaging.[19] Furthermore, the magnification is useful for improving spatial resolution[20,21] in digital radiography, and the image quality is improved by decreasing scattering X-ray intensity from an object. Because most microfocus X-ray tubes employ tungsten targets, gadolinium K-edge angiography can be performed using tungsten Kα rays.

In the present research, we employed a 100-μm-focus X-ray generator to perform a preliminary study on enhanced magnification angiography utilizing gadolinium media by decreasing bremsstrahlung X-ray intensity.

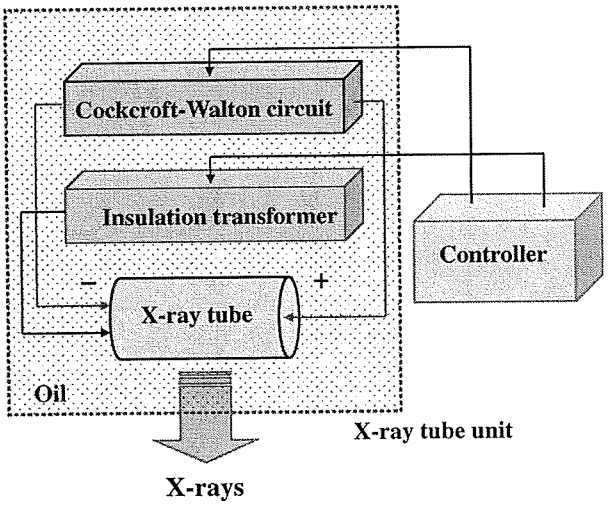

Fig. 1. Block diagram of 100-μm-focus X-ray generator.

2. X-ray Generator

Figure 1 shows the block diagram of a microfocus X-ray generator used in this experiment, and the generator consists of a main controller and an X-ray tube unit with a 100-μm-focus tube. Tube voltage, current, and exposure time can be controlled using the controller. The high-voltage line employs the Cockcroft–Walton circuit in order to decrease the dimensions of the tube unit. In the X-ray tube unit, the positive and negative high voltages are applied to the anode and cathode electrodes, respectively. The filament heating current is supplied by an AC power supply in the controller in conjunction with an insulation transformer, which is used for isolation from the high voltage from the Cockcroft–Walton circuit. In this experiment, the tube voltage applied was from 80 to 106 kV, and the tube current was regulated to be within 0.50 mA (maximum current) by filament temperature. Exposure time is controlled in order to obtain optimum X-ray intensity, and K-series characteristic X-rays are selected out using a 100-μm-thick tungsten filter.

To design a tungsten K-edge filter, the transmittance T of Kα rays is given by

$$T = I/I_0 = \exp[-\mu(\varepsilon) \cdot \xi] \approx 0.5, \quad (1)$$

where I is the transmission Kα intensity, I_0 is the incident Kα intensity, $\mu(\varepsilon)$ is the linear absorption coefficient at an average photon energy ε of Kα rays, and ξ is the filter thickness (half-value layer). Thus, ξ is calculated as approximately 100 μm and is written as

$$\xi = \log 2/[\mu_w(\varepsilon) \cdot \rho] \approx 100\,\mu\text{m}, \quad (2)$$

where $\mu_w(\varepsilon)$ is the mass absorption coefficient of tungsten at an ε, and ρ is the tungsten density.

3. Results and Discussion

3.1 X-ray intensity

X-ray intensity was measured by a Victoreen 660 ionization chamber at 1.0 m from the X-ray source. At a constant tube current of 0.50 mA, X-ray intensity increased when tube voltage was increased. At a tube voltage of 100 kV, the intensity was substantially decreased using the filter, and the intensities without filtering and with filtering were 449 and 19.8 μGy/s, respectively (Fig. 2). Therefore, the absorbed dose in patients can be decreased using the filter for gadolinium angiography.

3.2 X-ray spectra

In order to measure X-ray spectra, we employed a cadmium telluride detector (Amptek XR-100T) using the filter (Fig. 3). When tube voltage was increased, the characteristic X-ray intensity increased, and both the maximum photon energy and the spectrum peak energy increased.

For gadolinium K-edge angiography, tungsten Kα rays are useful, and bremsstrahlung X-rays with energies below the gadolinium K-edge decrease the image contrast. Using this filter, because bremsstrahlung rays with energies higher than 100 keV were not absorbed easily, the tube voltage for angiography was determined as 100 kV by considering the filtering effect of an object.

3.3 Magnification radiography

Magnification radiography was performed by threefold magnification imaging using the CR system at a tube voltage

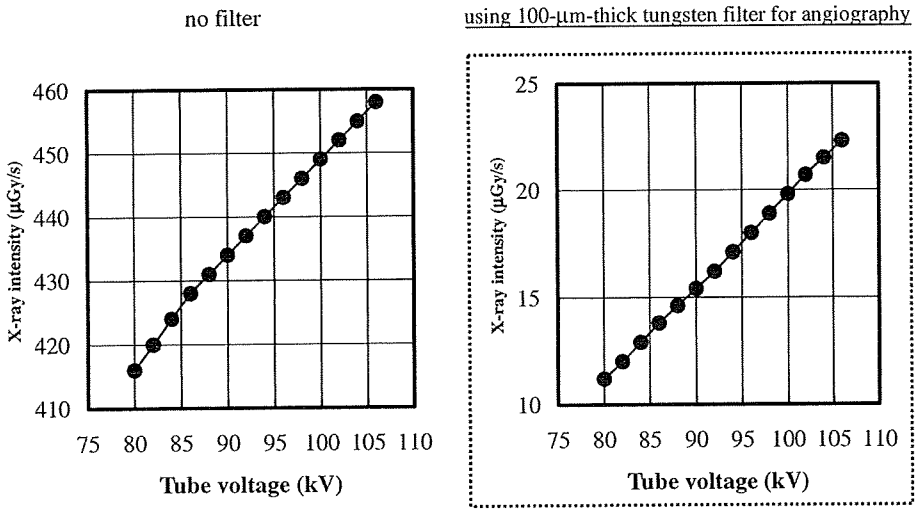

Fig. 2. X-ray intensities (μGy/s) at 1.0 m from source as function of tube voltage (kV) at tube current of 0.50 mA.

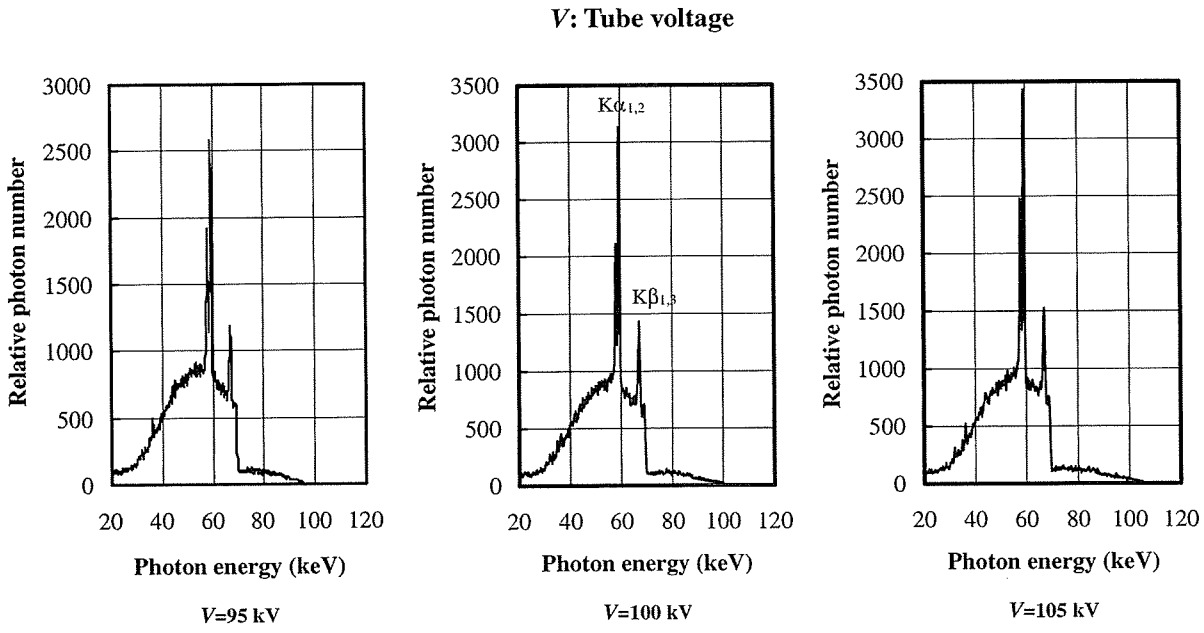

Fig. 3. X-ray spectra measured using 100-μm-thick tungsten filter with changes in tube voltage.

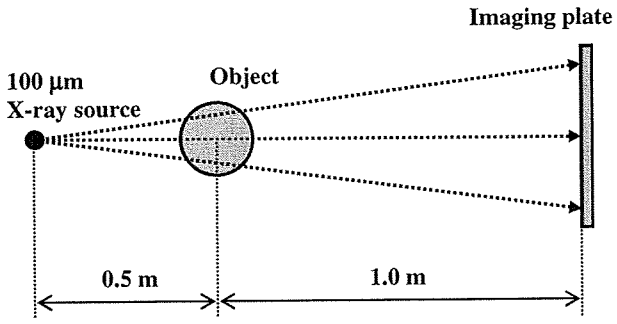

Fig. 4. Threefold magnification imaging using imaging plate.

of 100 kV, a tube current of 0.50 mA, and a distance of 1.5 m between the X-ray source and the imaging plate (Fig. 4). First, spatial resolution was measured using a lead test chart at an exposure time of 10 s. Although the spatial resolution of cohesion radiography was approximately 200 μm, 71-μm-thick lines (seven line pairs) were visible in magnification radiography (Fig. 5).

Figure 6 shows radiograms of a 50-μm-diameter tungsten wire coiled around a 30-mm-diameter rod made of poly(methyl methacrylate) (PMMA) at an exposure time of 10 s. Owing to the blurring of the image caused by a sampling pitch of 87.5 μm, the wire diameter in radiography was decreased utilizing magnification imaging. Although the tungsten wire transmitted tungsten K-rays easily, the contrast of the wire increased using the filter for absorbing bremsstrahlung rays, because low-photon-energy bremsstrahlung rays with energies below the K-edge were absorbed easily by the rod.

3.4 *Enhanced magnification angiography*

Figure 7 shows the mass attenuation coefficients of gadolinium at the selected energies; the coefficient curve is discontinuous at the gadolinium K-edge. The average photon energy of the tungsten Kα lines is shown above the gadolinium K-edge. The average photon energy of tungsten

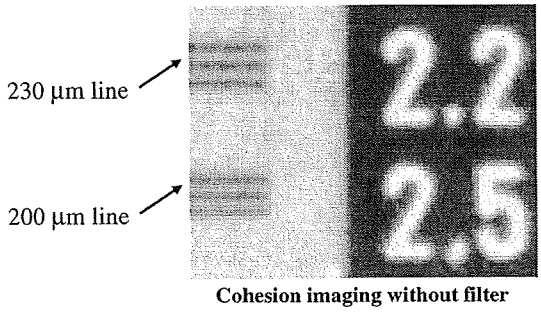

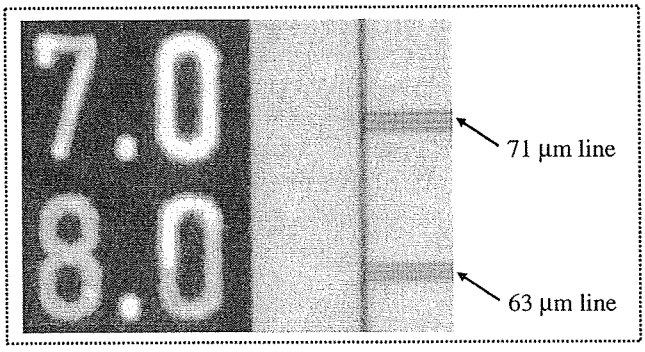

Fig. 5. Radiograms of test chart for measuring spatial resolution using filter.

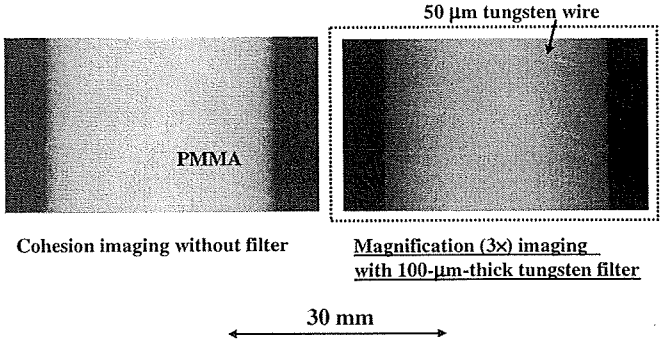

Fig. 6. Radiograms of tungsten wire coiled around PMMA rod.

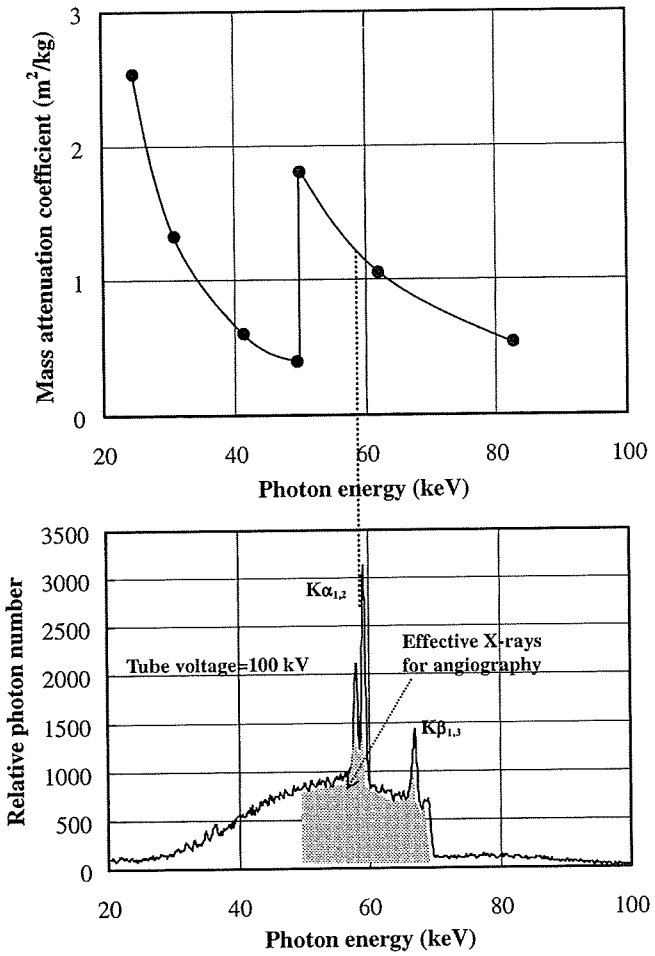

Fig. 7. Mass attenuation coefficients of gadolinium and average photon energy of tungsten Kα rays. Tungsten K-rays and bremsstrahlung rays with energies beyond the K-edge are absorbed effectively by gadolinium media.

Kα rays is 58.9 keV, and gadolinium contrast media with a K-absorption edge of 50.2 keV absorb the rays easily. Therefore, blood vessels are observed with high contrasts.

Magnification angiography was performed using the filter at a voltage of 100 kV, a current of 0.50 mA, a distance of 1.5 m, and a time of 10 s. Figure 8 shows angiograms of a polytetrafluoroethylene (Teflon) tube of 1.0 mm bore diameter in a PMMA case using a contrast medium (Magnevist) that contains 150 mg/mL gadolinium. When the filter was used, the image contrast of the 1.0 mm tube was high.

To carry out fundamental studies on angiography, we usually use animal phantoms utilizing iodine-based microspheres 15 μm in diameter. In the present study, because there were no ready-made gadolinium microspheres, we used gadolinium oxide microparticles of 1 to 10 μm in diameter. Figures 9 and 10 show angiograms of two regions in a rabbit head obtained using gadolinium oxide particles. Using the filter, the contrasts of molars substantially decreased, and fine blood vessels were visible (Fig. 9). Next, the contrasts of incisives decreased, and blood vessels were clearly observed using the filter. In addition, spatial resolution was improved utilizing magnification imaging (Fig. 10). In both figures, fine blood vessels of approximately 100 μm are visible by magnification imaging using the filter.

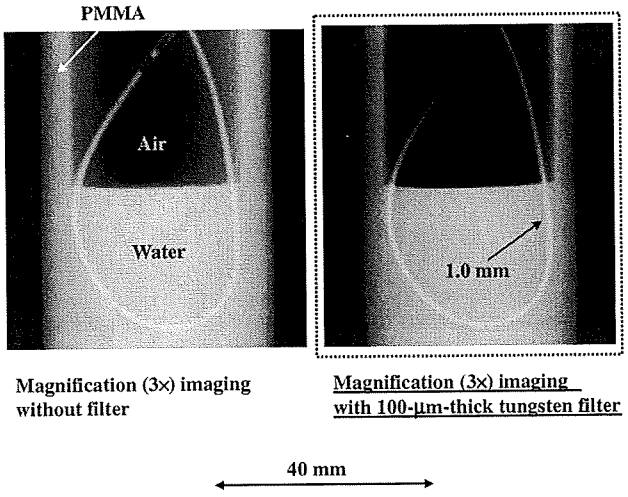

Fig. 8. Magnification angiograms of Teflon tube with bore diameter of 1.0 mm using a contrast medium (Magnevist) that contains approximately 150 mg/mL gadolinium.

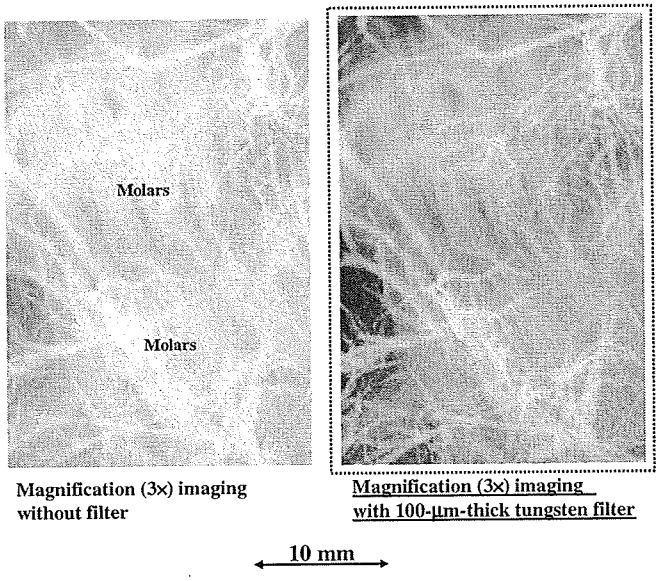

Fig. 9. Magnification angiograms of molar region in rabbit head using gadolinium oxide particles for making phantoms.

4. Conclusions and Outlook

We employed an X-ray generator with a 100-μm-focus tungsten tube and performed enhanced magnification angiography using K-series characteristic X-rays of tungsten and high-photon-energy bremsstrahlung X-rays with a tube voltage of 100 kV, which can be absorbed easily by gadolinium media. The characteristic X-ray intensity increased with tube voltage, and the tube voltage was determined as 100 kV to increase the image contrast. The contrast of blood vessels was improved by insertion of the 100-μm-thick tungsten filter for selecting out optimum X-rays. As compared with the dose without filtering, the exposure dose in patients can be reduced to a value below 5% using the filter without lowering image quality.

The spatial resolution of the CR system was approximately 200 μm, and the resolution was improved to 70 μm by threefold magnification imaging using a 100-μm-focus

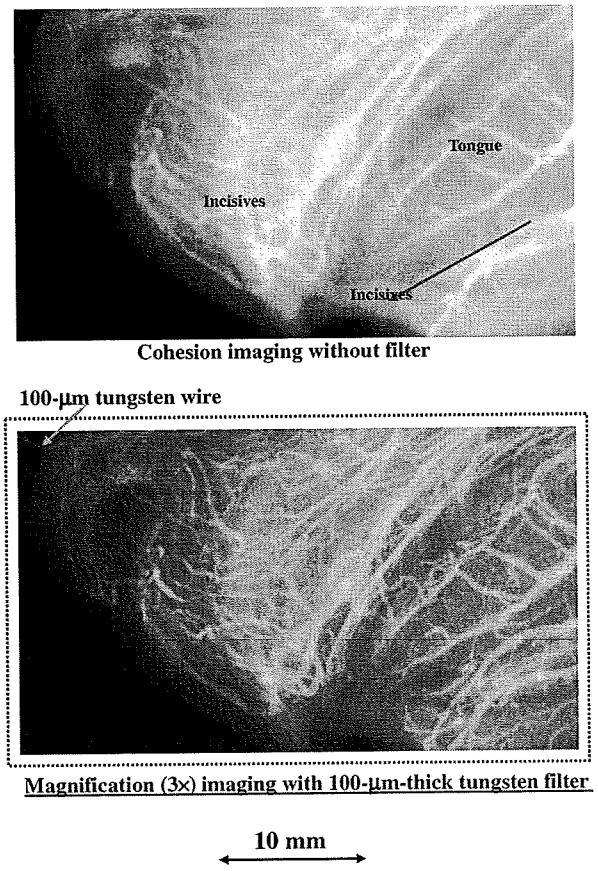

Fig. 10. Magnification angiograms of incisive region in rabbit head using gadolinium oxide particles.

tube. In order to clearly observe fine blood vessels below 100 μm in diameter, the sampling pitch of the CR system should be improved to 43.8 μm (Konica Minolta Regius 190). From experimental results, the maximum magnification rate without blurring was approximately threefold using a 100-μm-focus tube, and the rate increased with decreasing the focus diameter. In addition, the rate should be minimized to decrease the absorbed dose in patients.

Lately, we have developed several different X-ray nanoparticles such as quantum dots by wet dispersion. In particular, gadolinium-oxide nanoparticles can be used as x-ray-fluorescence and magnetic-resonance dots. In novel monochromatic X-ray imaging techniques utilizing drug delivery systems (DDSs), an X-ray fluorescence CT and a K-edge X-ray CT systems have been developed using grants from Japan Science and Technology Agency (JST). Therefore, we are very interested in molecular-level DDS imaging using several different nanoparticles.

At a tube voltage of 100 kV and a current of 0.50 mA, the maximum number of photons after penetrating the filter was approximately 5×10^7 photons·cm^{-2}·s^{-1} at 1.0 m from the source, and real time digital magnification radiography can be performed using an image intensifier camera (Hamamatsu C7716) with a frame rate of 30 frames per second (fps). To improve image quality and to increase frame rate using a flat panel detector, we have to increase count rate by increasing tube current, and photon count rate can be increased to 1×10^9 photons·cm^{-2}·s^{-1} at 1.0 m using a kilowatt-range 100-μm-focus tungsten tube with a rotating anode.

Acknowledgments

This work was supported by Grants-in-Aid for Scientific Research and Advanced Medical Scientific Research from MECSST, Health and Labor Sciences Research Grants, Grants from the Keiryo Research Foundation, Promotion and Mutual Aid Corporation for Private Schools of Japan, the Japan Science and Technology Agency (JST), and the New Energy and Industrial Technology Development Organization (NEDO).

1) A. C. Thompson, H. D. Zeman, G. S. Brown, J. Morrison, P. Reiser, V. Padmanabahn, L. Ong, S. Green, J. Giacomini, H. Gordon, and E. Rubenstein: Rev. Sci. Instrum. **63** (1992) 625.
2) H. Mori, K. Hyodo, E. Tanaka, M. Uddin-Mohammed, A. Yamakawa, Y. Shinozaki, H. Nakazawa, Y. Tanaka, T. Sekka, Y. Iwata, S. Handa, K. Umetani, H. Ueki, T. Yokoyama, K. Tanioka, M. Kubota, H. Hosaka, N. Ishikawa, and M. Ando: Radiology **201** (1996) 173.
3) K. Hyodo, M. Ando, Y. Oku, S. Yamamoto, T. Takeda, Y. Itai, S. Ohtsuka, Y. Sugishita, and J. Tada: J. Synchrotron Radiat. **5** (1998) 1123.
4) R. Germer: J. Phys. E **12** (1979) 336.
5) E. Sato, M. Sagae, E. Tanaka, Y. Hayasi, R. Germer, H. Mori, T. Kawai, T. Ichimaru, S. Sato, K. Takayama, and H. Ido: Jpn. J. Appl. Phys. **43** (2004) 7324.
6) E. Sato, E. Tanaka, H. Mori, T. Kawai, S. Sato, and K. Takayama: Opt. Eng. **44** (2005) 049002.
7) E. Sato, Y. Hayasi, R. Germer, E. Tanaka, H. Mori, T. Kawai, T. Inoue, A. Ogawa, S. Sato, K. Takayama, and J. Onagawa: Jpn. J. Appl. Phys. **45** (2006) 5301.
8) E. Sato, Y. Hayasi, E. Tanaka, H. Mori, T. Kawai, T. Inoue, A. Ogawa, S. Sato, K. Takayama, J. Onagawa, and H. Ido: Radiat. Phys. Chem. **75** (2006) 1812.
9) E. Sato, E. Tanaka, H. Mori, T. Kawai, T. Ichimaru, S. Sato, K. Takayama, and H. Ido: Med. Phys. **31** (2004) 3017.
10) E. Sato, E. Tanaka, H. Mori, T. Kawai, T. Inoue, A. Ogawa, A. Yamadera, S. Sato, F. Ito, K. Takayama, J. Onagawa, and H. Ido: Jpn. J. Appl. Phys. **44** (2005) 8204.
11) E. Sato, K. Sato, and Y. Tamakawa: Annu. Rep. Iwate Med. Univ. School Lib. Arts Sci. **35** (2000) 13.
12) E. Sato, Y. Hayasi, K. Kimura, E. Tanaka, H. Mori, T. Kawai, T. Inoue, A. Ogawa, S. Sato, K. Takayama, J. Onagawa, and H. Ido: Jpn. J. Appl. Phys. **44** (2005) 8716.
13) E. Sato, Y. Hayasi, E. Tanaka, H. Mori, T. Kawai, T. Inoue, A. Ogawa, S. Sato, K. Takayama, J. Onagawa, and H. Ido: Radiat. Phys. Chem. **75** (2006) 1841.
14) D. J. Spinosa, J. A. Kaufmann, and G. D. Hartwell: Radiology **223** (2002) 319.
15) J. W. Henson, R. G. Nogueira, D. J. Covarrubias, R. G. Gonzalez, and M. H. Lev: Am. J. Neuroradiol. **25** (2004) 969.
16) E. Sato, S. Nomiya, K. Hitomi, H. Onabe, T. Shoji, E. Tanaka, T. Kawai, T. Inoue, A. Ogawa, S. Sato, T. Ichimaru, and K. Takayama: Proc. SPIE **6706** (2007) 67060Y.
17) M. J. Bonvento, W. H. Moore, T. M. Button, H. J. Weinmann, R. Yakupov, and F. A. Dilmanian: Acad. Radiol. **13** (2006) 979.
18) T. Yu, X. Zhu, L. Tang, D. Wang, and N. Saad: Radiol. Clin. N. Am. **45** (2007) 461.
19) S. W. Wilkins, T. E. Gureyev, D. Gao, A. Pogany, and A. W. Stevenson: Nature **384** (1996) 335.
20) A. Ishisaka, H. Ohara, and C. Honda: Opt. Rev. **7** (2000) 566.
21) T. Enomoto, E. Sato, Y. Sumiyama, K. Aizawa, M. Watanabe, E. Tanaka, H. Mori, H. Kawakami, T. Kawai, T. Inoue, A. Ogawa, and S. Sato: Jpn. J. Appl. Phys. **45** (2006) 8005.

Radiol Phys Technol (2009) 2:46–53
DOI 10.1007/s12194-008-0042-1

X-ray fluorescence camera for imaging of iodine media in vivo

Hiroshi Matsukiyo · Manabu Watanabe · Eiichi Sato · Akihiro Osawa · Toshiyuki Enomoto · Jiro Nagao · Purkhet Abderyim · Katsuo Aizawa · Etsuro Tanaka · Hidezo Mori · Toshiaki Kawai · Shigeru Ehara · Shigehiro Sato · Akira Ogawa · Jun Onagawa

Received: 31 July 2008 / Revised: 30 September 2008 / Accepted: 1 October 2008 / Published online: 11 November 2008

Abstract X-ray fluorescence (XRF) analysis is useful for measuring density distributions of contrast media in vivo. An XRF camera was developed for carrying out mapping for iodine-based contrast media used in medical angiography. Objects are exposed by an X-ray beam from a cerium target. Cerium K-series X-rays are absorbed effectively by iodine media in objects, and iodine fluorescence is produced from the objects. Next, iodine Kα fluorescence is selected out by use of a 58-μm-thick stannum filter and is detected by a cadmium telluride (CdTe) detector. The Kα rays are discriminated out by a multichannel analyzer, and the number of photons is counted by a counter card. The objects are moved and scanned by an x–y stage in conjunction with a two-stage controller, and X-ray images obtained by iodine mapping are shown on a personal computer

H. Matsukiyo (✉) · M. Watanabe · A. Osawa · T. Enomoto · J. Nagao
The 3rd Department of Surgery,
Toho University School of Medicine,
2-17-6 Ohashi, Meguro-ku, Tokyo 153-8515, Japan
e-mail: hma2kiyo502leo@yahoo.co.jp

E. Sato
Department of Physics, Iwate Medical University,
2-1-1 Nishitokuta, Yahaba 028-3694, Japan

P. Abderyim
Department of Computer and Information Sciences,
Faculty of Engineering, Iwate University,
4-3-5 Ueda, Morioka 020-8551, Japan

K. Aizawa
Tokyo Medical University, 6-1-1 Shinjyuku,
Shinjyuku-ku, Tokyo 160-8402, Japan

E. Tanaka
Department of Nutritional Science,
Faculty of Applied Bio-Science,
Tokyo University of Agriculture, 1-1-1 Sakuragaoka,
Setagaya-ku, Tokyo 156-8502, Japan

H. Mori
Department of Cardiac Physiology,
National Cardiovascular Center Research Institute,
5-7-1 Fujishirodai, Suita, Osaka 565-8565, Japan

T. Kawai
Electron Tube Division #2, Hamamatsu Photonics K.K.,
314-5 Shimokanzo, Iwata, Shizuoka 438-0193, Japan

S. Ehara
Department of Radiology, School of Medicine,
Iwate Medical University, 19-1 Uchimaru,
Morioka 020-8505, Japan

S. Sato
Department of Microbiology, School of Medicine,
Iwate Medical University, 19-1 Uchimaru,
Morioka 020-8505, Japan

A. Ogawa
Department of Neurosurgery, School of Medicine,
Iwate Medical University, 19-1 Uchimaru,
Morioka 020-8505, Japan

J. Onagawa
Department of Electronics, Faculty of Engineering,
Tohoku Gakuin University, 1-13-1 Chuo,
Tagajo, Miyagi 985-8537, Japan